

Calculating the motion of highly confined, arbitrary-shaped particles in Hele-Shaw channels

Bram Bet,^{1,*} Rumen Georgiev,² William Uspal,^{3,4} Huyesin Burak Eral,² René van Roij,¹ and Sela Samin¹

¹*Institute for Theoretical Physics, Center for Extreme Matter and Emergent Phenomena, Utrecht University, Princetonplein 5, 3584 CC Utrecht, The Netherlands*

²*Process and Energy Department, Delft University of Technology, Delft 2628 CD, The Netherlands*

³*Max Planck Institute for Intelligent Systems, Heisenbergstr. 3, 70569 Stuttgart, Germany*

⁴*Institut für Theoretische Physik, Universität Stuttgart, Pfaffenwaldring 57, D-70569 Stuttgart, Germany*

(Dated: November 11, 2018)

We combine theory, numerical calculations, and experiments to accurately predict the motion of anisotropic particles in shallow microfluidic channels, in which the particles are strongly confined in the vertical direction. We formulate an effective quasi-two-dimensional description of the Stokes flow around the particle via the Brinkman equation, which can be solved in a time that is two orders of magnitude faster than the three-dimensional problem. The computational speedup enables us to calculate the full trajectories of particles in the channel. To test our scheme, we study the motion of dumbbell-shaped particles that are produced in a microfluidic channel using ‘continuous flow lithography’. Contrary to what was reported in earlier work (Uspal *et al.*, Nature communications 4 (2013)), we find that the reorientation time of a dumbbell particle in an external flow exhibits a minimum as a function of its disk size ratio. This finding is in excellent agreement with new experiments, thus confirming the predictive power of our scheme.

I. INTRODUCTION

Microfluidic devices offer many applications, such as flow cytometry [2–4], separation of cells [5], DNA sequencing [6], or blood cell analysis [7]. In many applications, it is of paramount importance to control the position of the immersed particles. Often, focusing of particles in the channel is achieved by external fields or by flows induced by the channel geometry [8], while particle separation or sorting can also be realised by tuning electric fields [3, 9] or the channel geometry [5, 10–13]. Alternatively, the shape of the particle itself offers a different route to manoeuvring the particles in the channel [14]. The hydrodynamics of various particles in strong confinement has been extensively studied, for instance the motion of confined droplets [15, 16], (connected) disks [1, 17], and fibers [18]. However, as tunability increases with the complexity of the particle shapes, theoretical arguments on the basis of simplified geometries might fall short of accurately describing the motion of particles. In addition, advances in versatile particle synthesis techniques, such as continuous-flow lithography [19], make an infinite variety of quasi-two-dimensional shapes experimentally accessible.

Inspired by these advances, we develop in this work a method to calculate the two-dimensional motion of confined particles in microfluidic channels that can handle particles of any given quasi-two-dimensional shape. Here, we combine finite-element calculations with a simple approach for the particle motion to solve the full hydrodynamic equations at hand, either in full detail in the three-dimensional geometry or in an effective two-dimensional description. Our method is validated by comparison of the three- and two-dimensional results with analytical calculations. Next, we apply our method to study dumbbell-shaped particles in Hele-Shaw channels, reproducing new experimental results accurately, without any adjustable parameters.

II. THEORY & NUMERICAL METHODS

A. Hydrodynamic equations and equations of motion

We consider a rigid particle, of arbitrary shape, at position $\mathbf{r}_p = (x_p, y_p, z_p)$, which is immersed in a fluid that is driven through a shallow microfluidic channel by the application of pressure at the channel inlet, see the illustration in Fig. 1. Let us assume that this particle is strongly confined in the z -direction, i.e. the particle is separated from

* B.p.bet@uu.nl

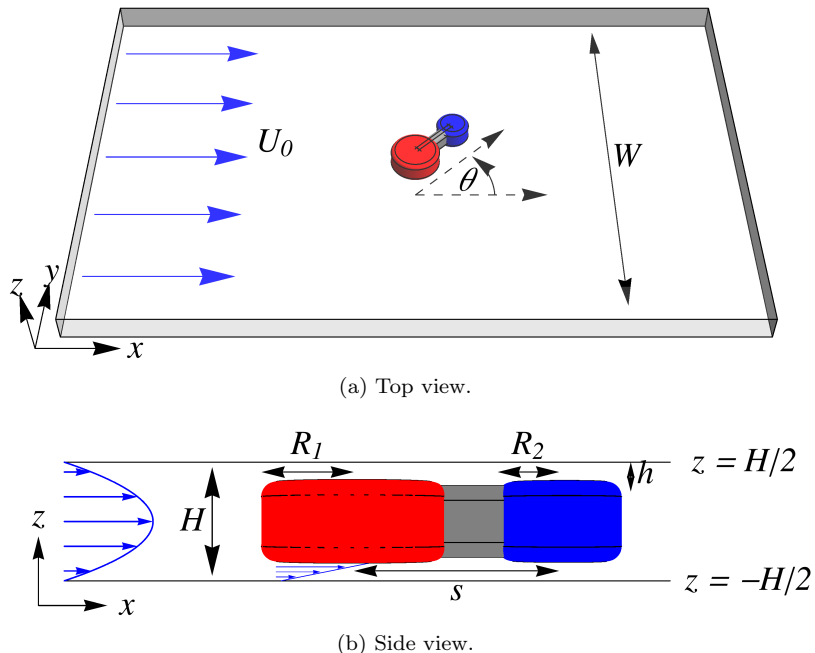


Figure 1. Top view (a) and side view (b) of the geometry and the Cartesian frame. An external flow \mathbf{U}_0 with parabolic profile is imposed through a channel of length L , width W and height H , containing a dumbbell particle with radii R_1 and R_2 at a center-to-center distance s , with height $H - 2h$, such that the height of the gaps between the particle and the top and bottom walls is given by h . In these gaps, the flow profile is approximately that of a simple shear flow. The orientation of the long axes of the dumbbell with respect to the external flow \mathbf{U}_0 is denoted by θ .

the top and bottom wall by a small gap of height h that is much smaller than the channel height H . Such a particle can be produced, for example, using ‘continuous flow lithography’ [19]. In this method, the fluid in the channel is a pre-polymer solution, where particles are ‘printed’ by cross-linking the oligomers by pulses of UV light, which is applied through a photolithographic mask. In this way, the particle shape is defined in the xy -plane by the shape of the mask (which can be of any desired shape), while it is extruded in the z -direction to a height that is comparable to the channel height, such that $h \ll H$.

The microfluidic channel under consideration here (see Appendix A) has a height $H = 30 \mu\text{m}$ and a much larger width $W = 500 \mu\text{m}$, while the length L of the channel is of the order of one centimeter, which can be considered infinite for our analysis. The fluid is driven through the channel at an average velocity U_0 , which is of the order of $50 \mu\text{m s}^{-1}$. Using the hydraulic diameter $D_H = 2HW/(H + W)$ as the characteristic length scale, we find that the Reynolds number is $\text{Re} = \rho U_0 D_H / \eta = 10^{-4} - 10^{-5}$ for a typical oligomer solution with viscosity η and density ρ . Therefore, the flow is well described by the Stokes equation [20–22]:

$$-\nabla p + \eta \nabla^2 \mathbf{u} = 0, \quad \nabla \cdot \mathbf{u} = 0, \quad (1)$$

where $\mathbf{u}(\mathbf{r})$ and $p(\mathbf{r})$ are the fluid velocity and pressure at position \mathbf{r} , respectively, and η denotes the fluid viscosity. We supplement the Stokes equation with no-slip boundary conditions on the (stationary) channel walls and the (moving) particle surface S_p ,

$$\mathbf{u}|_{\text{walls}} = 0, \quad \mathbf{u}|_{\mathbf{r} \in S_p} = \mathbf{U}_p + \boldsymbol{\omega}_p \times (\mathbf{r} - \mathbf{r}_p), \quad (2)$$

where \mathbf{U}_p and $\boldsymbol{\omega}_p$ denote the particle velocity and angular velocity, respectively. At the inlet of the channel, we impose a uniform incoming Hele-Shaw flow

$$\mathbf{u}|_{\text{inlet}} = \mathbf{U}_0(\mathbf{r}) = \frac{3}{2} \left(1 - \frac{4z^2}{H^2} \right) (U_0, 0, 0), \quad (3)$$

which is the analytic solution for the flow between two infinite parallel plates driven by a constant pressure difference. Here, $z \in [-H/2, H/2]$ and U_0 is the average velocity in the x -direction. Note that this boundary condition neglects

the no-slip condition on the sidewalls, i.e., it is not accurate close to the side walls. Therefore, we take into account a finite ‘entrance length’ at the inlet after which the flow is fully developed downstream in the channel. Finally, we impose a zero pressure boundary condition at the outlet, such that the pressure difference between inlet and outlet is precisely driving the flow field given by Eq. (3), i.e., $U_0 = -H^2 \nabla p / (12\eta)$. The influence of the no-slip side walls on this pressure drop is assumed to be negligible. The Stokes equation (1), together with these boundary conditions, form a closed set of equations that we solve numerically by a finite-elements scheme (see Section II C).

The fluid in the channel surrounding the particle exerts a hydrodynamic force \mathbf{F} and torque \mathbf{T} on the particle, which is calculated by integrating the hydrodynamic stress tensor, $\sigma_{ij} = -p\delta_{ij} + \eta(\partial_i u_j + \partial_j u_i)$, over the particle surface:

$$\mathbf{F} = \int_{S_p} dS \, \sigma \cdot \mathbf{n}, \quad \mathbf{T} = \int_{S_p} dS \, (\mathbf{r} - \mathbf{r}_p) \times (\sigma \cdot \mathbf{n}). \quad (4)$$

Due to the linearity of the Stokes equation (1), we can write the solution (p, \mathbf{u}) of Eq. (1) with boundary conditions (2) and (3) as a superposition of two solutions [21]: $\mathbf{u} = \mathbf{u}_0 + \mathbf{u}'$ and $p = p_0 + p'$, where (p_0, \mathbf{u}_0) and (p', \mathbf{u}') are solutions to the Stokes equation (1) with boundary conditions

$$\mathbf{u}_0|_{\text{walls}} = 0, \quad \mathbf{u}_0|_{\text{inlet}} = \mathbf{U}_0(\mathbf{r}), \quad \mathbf{u}_0|_{\mathbf{r} \in S_p} = 0; \quad (5)$$

$$\mathbf{u}'|_{\text{walls}} = 0, \quad \mathbf{u}'|_{\text{inlet}} = 0, \quad \mathbf{u}'|_{\mathbf{r} \in S_p} = \mathbf{U}_p + \boldsymbol{\omega}_p \times (\mathbf{r} - \mathbf{r}_p), \quad (6)$$

that is, \mathbf{u}_0 is the solution where the particle is fixed subject to the imposed external flow, and \mathbf{u}' the solution where the particle moves through the channel without an imposed flow. The stress tensor also splits accordingly, $\sigma = \sigma_0 + \sigma'$, such that we find that the forces and torque on the particle are written as $\mathbf{F} = \mathbf{F}_0 + \mathbf{F}'$ and $\mathbf{T} = \mathbf{T}_0 + \mathbf{T}'$, which are calculated from Eq. (4) by replacing σ with σ_0 or σ' .

To proceed, we can again use the linearity of the Stokes equation (1) to derive that the force \mathbf{F}' and torque \mathbf{T}' depend linearly on each component of the particle (angular) velocity via a 6×6 resistance tensor \mathcal{R} as [21, 23, 24]

$$\begin{pmatrix} \mathbf{F}' \\ \mathbf{T}' \end{pmatrix} = -\eta \mathcal{R} \begin{pmatrix} \mathbf{U}_p \\ \boldsymbol{\omega}_p \end{pmatrix}. \quad (7)$$

Due to the over-damped nature of the system, the (hydrodynamic) force and torque on the particle vanish in the absence of external forces on the particle. Therefore, after summing up the force contributions from the solutions \mathbf{u}_0 and \mathbf{u}' , we find that the particle must obey the equation of motion

$$\begin{pmatrix} \mathbf{F} \\ \mathbf{T} \end{pmatrix} = -\eta \mathcal{R} \begin{pmatrix} \mathbf{U}_p \\ \boldsymbol{\omega}_p \end{pmatrix} + \begin{pmatrix} \mathbf{F}_0 \\ \mathbf{T}_0 \end{pmatrix} = \begin{pmatrix} \mathbf{0} \\ \mathbf{0} \end{pmatrix}, \quad (8)$$

with $\mathbf{0} = (0, 0, 0)$. Thus, once \mathcal{R} , \mathbf{F}_0 and \mathbf{T}_0 are determined, either analytically or numerically, the equations of motion (8) can be solved for the particle velocity and angular velocity as

$$\begin{pmatrix} \mathbf{U}_p \\ \boldsymbol{\omega}_p \end{pmatrix} = \frac{1}{\eta} \mathcal{R}^{-1} \begin{pmatrix} \mathbf{F}_0 \\ \mathbf{T}_0 \end{pmatrix}. \quad (9)$$

Notice that \mathcal{R} , \mathbf{F}_0 and \mathbf{T}_0 depend on the position and orientation of the particle, such that Eq. (9) only determines the force- and torque-free (angular) velocity for that specific particle position and velocity. The position dependence of \mathcal{R} is related to the effects of the side walls; in the case of an infinite slit, the tensor \mathcal{R} will only depend on the particle geometry and its orientation (with respect to the imposed external flow).

In this work, due to the strong confinement in the vertical direction as well as the mirror symmetry in the $z = 0$ plane of the problem at hand, the movement of the particle is restricted to the two-dimensional mid-plane of the channel at $z = 0$, thereby reducing the number of degrees of freedom to three: $\mathbf{U}_p = (U_{p,x}, U_{p,y}, 0)$ and $\boldsymbol{\omega}_p = (0, 0, \omega_p)$, and similarly $\mathbf{F} = (F_x, F_y, 0)$ and $\mathbf{T} = (0, 0, T)$ [25]. Moreover, the particle position is determined by the coordinates (x_p, y_p) , while its orientation is described by a single angle θ , as illustrated in Fig. 1. Finally, the resistance tensor \mathcal{R} reduces to a 3×3 tensor, which is obtained from the relevant components of the original 6×6 resistance tensor. In some cases, symmetry arguments may be invoked to reduce the number of degrees of freedom even further, e.g. mirror symmetric particles that are aligned with the imposed external flow, as we shall see below.

Using a finite-elements scheme we can numerically solve the flow field \mathbf{u} for any imposed velocity and angular velocity, and from these solutions obtain the resistance tensor \mathcal{R} , the force \mathbf{F}_0 and the torque \mathbf{T}_0 , to subsequently obtain the force- and torque-free velocities from Eq. (9). By repeating this at the new particle position in the next time step, it is in principle possible to integrate the complete particle motion.

B. Brinkman equation

A three-dimensional finite-elements calculation is able to resolve the flow in the channel. However, due to a separation of length scales, $h \ll W$, the finite-element mesh needs to be chosen very fine at certain places, causing the calculations to be computationally costly, and eventually prohibitive for the purpose of integrating the particle motion. To circumvent this problem, we resort to an effective 2D-description of the system via the Brinkman equation [26, 27].

Far enough from the side walls and the particle, the flow field is well described by Hele-Shaw flow:

$$\mathbf{u}(x, y, z) = \frac{3}{2} \bar{\mathbf{u}}(x, y) \left(1 - \frac{4z^2}{H^2}\right), \quad (10)$$

the pressure being independent of z to a good approximation: $p = p(x, y)$. We substitute this ansatz in the Stokes equation (1) and average over the channel height to find the Brinkman equation [26, 27]

$$-\nabla_{2D} \bar{p} + \eta H \nabla_{2D}^2 \bar{\mathbf{u}} - \frac{12\eta}{H} \bar{\mathbf{u}} = 0, \quad \nabla_{2D} \cdot \bar{\mathbf{u}} = 0, \quad (11)$$

where the two-dimensional vector field $\bar{\mathbf{u}} = (\bar{u}_x, \bar{u}_y)$ denotes the z -averaged value of the three-dimensional flow field \mathbf{u} , and $\bar{p} = pH$ denotes the two-dimensional pressure field. Henceforth, we will denote the two-dimensional height-averaged quantities with an overbar. The boundary conditions that supplement Eq. (11) are accordingly:

$$\bar{\mathbf{u}}|_{\text{walls}} = 0, \quad \bar{\mathbf{u}}|_{\text{inlet}} = U_0 \hat{\mathbf{x}}, \quad \bar{\mathbf{u}}|_{(x,y) \in \partial \bar{S}_p} = \mathbf{U}_p + \omega_p (-y - y_p, x - x_p), \quad (12)$$

where $\mathbf{r} = (x, y)$ and $\partial \bar{S}_p$ denotes the one-dimensional particle boundary of the projected particle surface \bar{S}_p . Notice that the walls in this situation are the projections of the sidewalls at $y = \pm W/2$. As before, $\mathbf{U}_p = (U_{p,x}, U_{p,y})$ and ω_p denote the particle velocity and angular velocity, respectively.

The solution $(\bar{p}, \bar{\mathbf{u}})$ of the Brinkman equation (11) defines a stress tensor

$$\bar{\sigma}_{ij} = -\delta_{ij} \bar{p} + \eta H (\partial_i \bar{u}_j + \partial_j \bar{u}_i), \quad (13)$$

which is integrated over the particle surface to find the hydrodynamic force and torque on the particle:

$$\mathbf{F}_f = \int_{\partial \bar{S}_p} ds \bar{\sigma} \cdot \mathbf{n}, \quad T_f = \int_{\partial \bar{S}_p} ds \left((x - x_p) (\bar{\sigma} \cdot \mathbf{n})_y - (y - y_p) (\bar{\sigma} \cdot \mathbf{n})_x \right). \quad (14)$$

The subscript ‘ f ’ indicates that this is the force and torque due to the surrounding two-dimensional fluid, and *does not* include the force and torque from the confining walls.

Similar to the Stokes equation, the Brinkman equation is linear in the fields \bar{p} and $\bar{\mathbf{u}}$. Using a similar decomposition as in the previous section, we prove explicitly in Appendix C that the force \mathbf{F}_f and torque T_f admit a linear relation to the particle velocity and angular velocity in terms of a 3×3 resistance tensor \mathcal{R}_f :

$$\begin{pmatrix} \mathbf{F} \\ T \end{pmatrix}_f = -\eta \mathcal{R}_f \begin{pmatrix} \mathbf{U}_p \\ \omega_p \end{pmatrix} + \begin{pmatrix} \mathbf{F}_0 \\ T_0 \end{pmatrix}. \quad (15)$$

In Appendix C, it is shown that that \mathcal{R}_f is symmetric by employing a version of the Lorentz reciprocal theorem for solutions of the Brinkman equation, which is given in Appendix B.

Since the fluid-filled gaps between the particle and the walls are not accounted in the Brinkman description, their contribution to the force and torque on the particle, which stem from the friction with the top and bottom wall, are missing. To obtain this contribution, we assume locally a simple shear flow in the narrow gaps between the particle and the confining walls. As a result, an area element dS on either of the particle faces that moves with a velocity $\mathbf{v}_S = \mathbf{U}_p + \omega_p \times (\mathbf{r} - \mathbf{r}_p)$ with respect to the wall, will experience a friction force $\mathbf{f}_S = -(\eta/h) \mathbf{v}_S dS$. The total force \mathbf{F}_w on the particle due to the wall friction is then found by integrating over the particle-gap surface,

$$\mathbf{F}_w = -\frac{2\eta}{h} \int_{\bar{S}_p} dS (\mathbf{U}_p + \omega_p \times (\mathbf{r} - \mathbf{r}_p)), \quad (16)$$

where the factor 2 is due to the two gaps. The area element dS also generates a torque $\mathbf{r} \times \mathbf{f}_S$, which can be integrated to find the frictional torque on the particle due to the walls:

$$\mathbf{T}_w = -\frac{2\eta}{h} \int_{\bar{S}_p} dS \left((\mathbf{r} - \mathbf{r}_p) \times (\mathbf{U}_p + \omega_p \times (\mathbf{r} - \mathbf{r}_p)) \right). \quad (17)$$

As before, the linear dependence of Eqs. (16) and (17) in the particle velocities leads to

$$\begin{pmatrix} \mathbf{F} \\ T \end{pmatrix}_w = -\eta \mathcal{R}_w \begin{pmatrix} \mathbf{U}_p \\ \omega_p \end{pmatrix}, \quad (18)$$

where the components of the 3×3 wall resistance tensor \mathcal{R}_w are calculated from (16) and (17) to be

$$\mathcal{R}_{w,11} = \mathcal{R}_{w,22} = \frac{2}{h} \int_S dS; \quad (19)$$

$$\mathcal{R}_{w,12} = \mathcal{R}_{w,21} = 0; \quad (20)$$

$$\mathcal{R}_{w,13} = \mathcal{R}_{w,31} = \frac{2}{h} \int_S dS (-y); \quad (21)$$

$$\mathcal{R}_{w,23} = \mathcal{R}_{w,32} = \frac{2}{h} \int_S dS x; \quad (22)$$

$$\mathcal{R}_{w,33} = \frac{2}{h} \int_S dS (x^2 + y^2). \quad (23)$$

Here, the off-diagonal components of the symmetric tensor \mathcal{R}_w are explicit manifestations of hydrodynamic rotation-translation coupling for anisotropic particles, which vanish for particles with enough symmetry [1].

Taking Equations (15) and (18) together, we find the same force balance that was obtained above, but with an explicit specification of the fluid and wall contributions:

$$\begin{pmatrix} \mathbf{F} \\ T \end{pmatrix} = -\eta \mathcal{R} \begin{pmatrix} \mathbf{U}_p \\ \omega_p \end{pmatrix} + \begin{pmatrix} \mathbf{F}_0 \\ T_0 \end{pmatrix} = \begin{pmatrix} \mathbf{0} \\ 0 \end{pmatrix}, \quad (24)$$

with $\mathcal{R} = \mathcal{R}_f + \mathcal{R}_w$ the symmetric 3×3 overall resistance tensor. The accuracy of this equality is directly related to the accuracy of the assumptions underlying the Brinkman equation and the simple shear flow in the gaps. Notice that Eq. (24) is equivalent to Eq. (9), indicating that this result is not sensitive to the hydrodynamic model one chooses for the hydrodynamic fluid-particle interaction, because of the overdamped nature of the system and the fact that there are no external force and torque acting on the particle.

C. Numerical methods

The Stokes equation (1) or the Brinkman equation (11) can be solved numerically for a particle of any shape in the channel. In this work, we use the finite-elements software COMSOL Multiphysics (COMSOL, Inc., Burlington, MA, USA) to find the flow field \mathbf{u} or $\bar{\mathbf{u}}$. Using this solution, we can determine the forces acting on the particle and integrate its motion using a numerical scheme detailed below.

At a given particle position (x_p, y_p) and orientation θ , each column of the resistance tensor \mathcal{R} is determined by imposing a single non-zero component of the particle velocities (\mathbf{U}_p, ω_p) , without external flow. The force and torque that determine the column of \mathcal{R} are either found by numerically solving the Stokes equation (1) and integrating the obtained stress tensor via Eq. (4), or by solving the Brinkman equation (11) and integrating via Eq. (14) and Eqs. (19) - (23). Similarly, \mathbf{F}_0 and T_0 are found by fixing the particle in the external flow, in either formalism.

With \mathcal{R} , \mathbf{F}_0 and T_0 determined from the finite elements solutions, the force- and torque-free velocity $\mathbf{U}_p(x, y, \theta)$ and angular velocity $\omega_p(x, y, \theta)$ are calculated from Eq. (24). Then, the particle position and orientation are integrated as

$$x(t + \Delta t) = x(t) + U_{p,x}(x(t), y(t), \theta(t)) \Delta t \quad (25)$$

$$y(t + \Delta t) = y(t) + U_{p,y}(x(t), y(t), \theta(t)) \Delta t \quad (26)$$

$$\theta(t + \Delta t) = \theta(t) + \omega_p(x(t), y(t), \theta(t)) \Delta t, \quad (27)$$

for some appropriately chosen time step Δt . The inversion of \mathcal{R} to obtain the solution of Eq. (24), and the numerical integration (25) - (27) are performed in MATLAB to obtain the position and orientation at the next time step, which are subsequently fed back into the finite-elements calculations.

D. Validity of the Brinkman equation

To test the validity of the Brinkman formalism described above, we compare with results obtained from three-dimensional analytical or numerical solutions of the Stokes equation. Here, we do this by considering the terminal

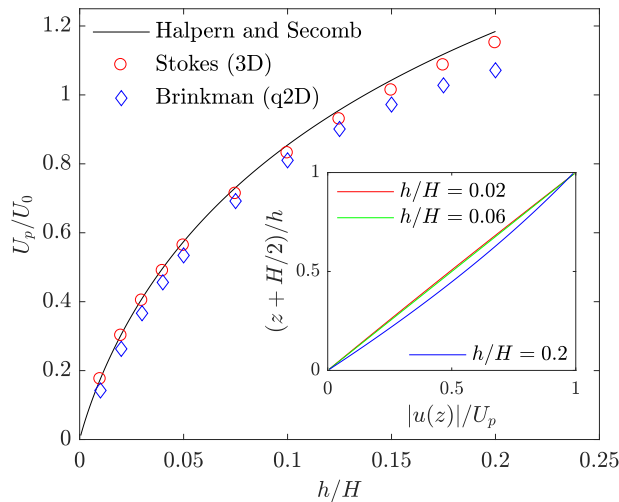


Figure 2. Terminal velocity of a rounded cylinder between two confining plates. The radius of the cylinder is $R/H = 1.79(1 - 2h/H) + r_c$, with radius of curvature $r_c = (H - 2h)/2$ for the rounded edges, where H and h are the channel and gap height, respectively. The inset shows the z -dependence of the flow field magnitude $|u(z)|$ relative to the particle velocity U_p , at position $x = y = 0$ in the thin gap between the bottom wall (at $z = -H/2$) and the particle disk surface (at $z = -H/2 + h$), for different gap heights h .

velocity of a disk that is moving with the fluid between two infinite parallel plates (corresponding to the experimental setup but with W large compared to the disk size), for which an analytical result by Halpern and Secomb exists [28]. The analysis in Ref. [28] concerns a cylindrical disk with rounded edges with a radius of curvature that is precisely half the height of the cylinder. In Fig. 2, we plot the particle velocity U_p , scaled by U_0 , as a function of the gap height h/H . We compare the analytical solution to the results obtained from the solutions of the Stokes equation and of the Brinkman equation. We find good agreement between the three calculations, especially for smaller gaps. The deviations at larger gaps are expected, since the assumption of a simple shear flow and the quasi-2D character ceases to hold in this region. To test this, we plot in the inset of Fig. 2 the magnitude of the flow field in the thin gap between the bottom wall at $z = -H/2$, where we have $|\mathbf{u}| = 0$, and the disk surface at $z = -H/2 + h$, where $|\mathbf{u}| = U_p$. We find that, for $h/H = 0.02$, the dependence of the flow field on the height z is linear, corresponding to simple Couette flow. Conversely, for $h/H = 0.2$, we find a deviation from the linear dependence, indicating that the simple shear flow assumption ceases to hold. The case of $h/H = 0.06$ corresponds to the experiments in this work, where from Fig. 2 we see that the simple shear flow assumption is still valid.

It should be noticed that the rounding of cylinder edges is not taken into account in the quasi-2D calculations. This does not seem to influence the results strongly, since the results agree with the analytical and three-dimensional numerical results where the rounded edges are taken into account. An attempt to incorporate rounded edges, by making the gap height in our quasi-2D calculations position-dependent, did not improve the results significantly, but increased the computational time by a factor two and was therefore not continued.

III. RESULTS

To test our numerical scheme for complex particle geometries, where analytical solutions are not available, we turn our attention to the situation described by Uspal *et al.* [1]. In Ref. [1] and in this work, dumbbell-shaped particles are produced in the channel using ‘continuous flow lithography’. These dumbbell particles consist of two circular disks of radius R_1 and $R_2 \leq R_1$, respectively, and height $H - 2h$. The smaller disk has a fixed radius $R_2 = 18.75 \mu\text{m}$, while the larger disk radius R_1 is varied. The disks are connected, at a fixed center-to-center distance $s = 62.5 \mu\text{m}$, by a cuboid of width $13.7 \mu\text{m}$, which has the same height as the two disks. In the experiments, the dumbbell edges are not completely sharp but are rounded, with a rounding radius $r_c/H = 0.15$, as estimated from experimental images [1]. This detail is incorporated in the three-dimensional calculations, but not in the two-dimensional calculations. The particle geometry is depicted in Fig. 1b.

In this work, we focus on the aligning motion observed in Ref. [1], where asymmetric dumbbells oriented in the flow with the larger disk upstream. The orientation θ between the long axis of the dumbbell and the flow direction

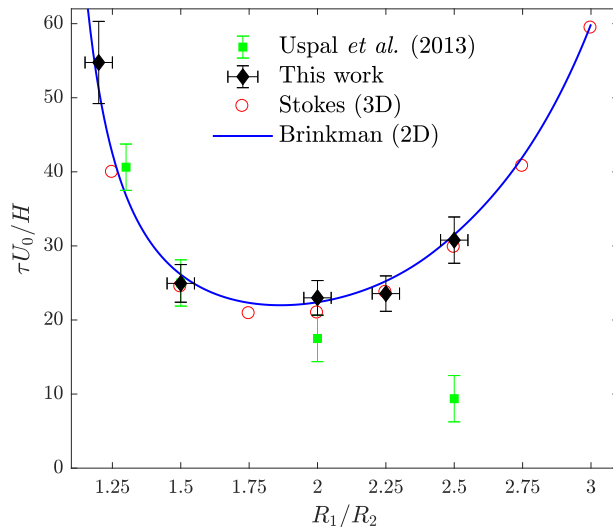


Figure 3. The characteristic reorientation time τ for dumbbell particles, as obtained from 3D finite-elements method in the Stokes formalism (red) and 2D finite-elements in the Brinkman formalism (blue), and experimental data from the previous experiments of Ref. [1] (green) and new experiments (black), as a function of R_1/R_2 .

(see Fig. 1a) was shown to follow the equation

$$\dot{\theta} = -\frac{1}{\tau} \sin \theta, \quad (28)$$

where the characteristic timescale τ is dependent on the particle geometry. Specifically, we investigate here the dependence of τ on the ratio of the disk radii R_1/R_2 . From Eq. (28), we see that τ can be obtained from a trajectory by considering the angular velocity at perpendicular orientation:

$$\tau = -\frac{1}{\dot{\theta}(\theta = \pi/2)}. \quad (29)$$

Hence, we can use the 3D and quasi-2D calculations described above to find the angular velocity of a particular dumbbell and obtain τ through (29).

The results are shown in Fig. 3, where we plot τ against R_1/R_2 . In green squares, we show the experimental data of [1]; the red circles show the numerical data from our three-dimensional calculations, while the blue line shows the results from the quasi-two-dimensional calculations. Firstly, we observe excellent agreement between the numerical results, which serves as another confirmation of the validity of our quasi-two-dimensional calculations. Secondly, we see that the results agree with the previous experimental data, with the exception of the data point of the most asymmetric size ratio $R_1/R_2 = 2.5$. Our calculations clearly show that a minimum in τ is expected around $R_1/R_2 \approx 1.9$, with τ increasing for larger R_1/R_2 .

In contrast, the previous data show a strictly decreasing dependence of τ on R_1/R_2 . Moreover, the theoretical curve that was fitted to the data in Ref. [1] was monotonically decreasing. This curve was derived considering an idealized situation of a pair of disks connected with a massless rod, which demonstrates the pitfalls of oversimplifying the geometry. However, we argue here that the minimum for τ that is predicted by our analysis is correct. In our calculations, as well as in the experiments, R_1/R_2 is varied by varying R_1 , while keeping R_2 and the center-to-center distance s constant. As a result, when $R_1 \geq R_2 + s$, the shape becomes effectively just a single disk, which will not rotate at all ($\tau \rightarrow \infty$) due to symmetry (provided it is still in the center of the channel). Therefore, when $R_1/R_2 \rightarrow \infty$, we should have $\tau \rightarrow \infty$ and hence a minimum in τ . Note that the overlapping of the two disks is not incorporated in the theoretical results of Ref. [1].

To clear up this discrepancy, we performed a new set of experiments using an experimental setup that is almost identical to the setup in Ref. [1]. Dumbbell particles were produced in a Hele-Shaw channel using continuous flow lithography and their reorientation motion was tracked, as described in Appendix A. In our experimental setup, the particle geometry and gap heights are taken to be approximately identical to those used in Ref. [1]. Our measured reorientation times τ are shown by black diamonds in Fig. 3, where an excellent agreement with our numerical results is observed. The new data confirms the existence of a minimum in the τ as a function of R_1/R_2 . We stress that our

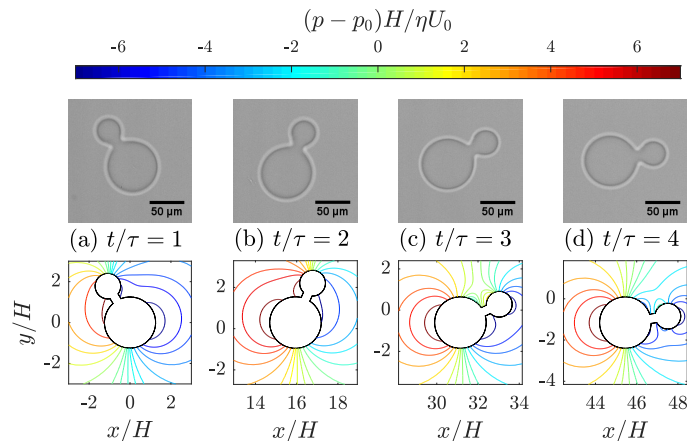


Figure 4. Experimental (top) and numerical (bottom) snapshots of the reorienting motion of a dumbbell with $R_1/R_2 = 2$ in the microfluidic channel, at $t/\tau = 1$ (a), $t/\tau = 2$ (b), $t/\tau = 3$ (c), $t/\tau = 4$ (d), where the initial orientation of the dumbbell is $\theta(0) = 5\pi/6$. We clearly observe that the dumbbell reorients with the larger disk upstream ($\theta = 0$). Around the dumbbell we show isobars of the disturbance pressure field created by the particle, as obtained from Eq. (11).

numerical method does not rely on any adjustable parameter, and uses only the experimental geometry and flow rate as input.

We have also calculated the complete angular trajectory of the dumbbell particles. Setting the time step to $\Delta t/\tau = 0.2$, we integrated the position and orientation as described in Eqs. (25) - (27), starting from an initial orientation $\theta(t = 0) = 5\pi/6$. Indeed, we observe that the dumbbells will align with the flow such that the larger disk is upstream ($\theta = 0$). This is illustrated in Fig. 4, where we contrast experimental (top) and numerical (bottom) snapshots of the reorienting particle at times $t/\tau = 1$ (a), $t/\tau = 2$ (b), $t/\tau = 3$ (c), and $t/\tau = 4$ (d). We do not distinguish here between the τ values obtained from experiment and numerical calculations, since the two results are found to agree very well. Around the particle in the numerical snapshots of Fig. 4, we show isobars of the disturbance pressure field $p(x, y) - p_0(x)$ created by the particle, which are obtained from the Brinkman equation (11) with the force- and torque-free (angular) velocity imposed. Here, p_0 denotes the pressure field corresponding to an undisturbed external flow U_0 in the channel. The contours of $p(x, y) - p_0(x)$ show the dipolar nature of the disturbance flow. A clear impression of the particle motion may be obtained from the microscopic movie and animations found in the supplemental material. [29]

The results for the complete angular trajectories are shown in Fig. 5. When time is rescaled by τ , we find a data collapse of the numerical calculations (open symbols) on the analytical solution of Eq. (28) (solid red line). This collapse offers a strong confirmation that the orientation is indeed correctly described by equation Eq. (28). For $R_1/R_2 = 2.0$, we have also calculated a complete trajectory using the three-dimensional method. The results, shown by the large blue circles in Fig. 5, perfectly agrees with the quasi-two-dimensional results, a final confirmation of the accuracy of our quasi-two-dimensional calculations. Finally, we also show an experimentally obtained trajectory (black dots), and find good agreement with the numerical results. Discrepancies may be attributed to small variations in the channel height due to fabrication imperfections or dust particles in the pre-polymer mixture.

IV. SUMMARY AND OUTLOOK

In conclusion, we have set up a combined theoretical and numerical framework that uses numerical solutions of either three-dimensional (Stokes) or quasi-two-dimensional (Brinkman) hydrodynamical equations, to calculate strongly confined particle motion in shallow microfluidic channels. Our method is not restricted to simplified shapes such as disks, but is able to handle any shape. The method is validated by comparing between analytical and three- and quasi-two-dimensional numerical calculations, which shows excellent agreement. The two orders of magnitude of computational speed-up that is offered by the quasi-two-dimensional description, enables to fully resolve the particle trajectory in time.

Our method is applied to dumbbell particles, for which we have calculated the characteristic rotation time τ as a function of R_1/R_2 , and found that, contrary to earlier findings, τ shows a minimum at $R_1/R_2 \simeq 1.9$. The existence of a minimum is confirmed by a new set of experiments. Moreover, we have calculated the angular motion as a function of time, and shown that it agrees with the equation of motion derived earlier, and with the trajectories that are

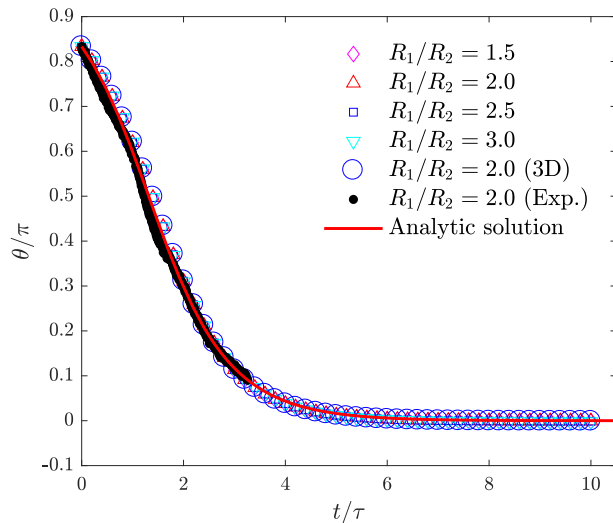


Figure 5. The orientation angle θ as a function of rescaled time t/τ , with $\theta(t=0) = 5\pi/6$, for dumbbells of varying R_1/R_2 . The large blue circles show the trajectory obtained using the three-dimensional method, while the black dots show one particular trajectory obtained from the experiments, both for a dumbbell particle with $R_1/R_2 = 2$. Errorbars for the experimental data are smaller than the black dots and hence omitted. The solid red line shows the analytical solution of equation (28).

obtained from the experiments.

In future work, it will be interesting to further investigate the relation between the geometry and the trajectories of different particles, with the goal to possibly steer particles to different areas in the channel. Lastly, our method is easily generalized to systems of multiple particles, which can offer a controlled setup to study hydrodynamic interaction between confined particles. Work in this direction is already under-way.

ACKNOWLEDGMENTS

This work is part of the D-ITP consortium, a program of the Netherlands Organisation for Scientific Research (NWO) that is funded by the Dutch Ministry of Education, Culture and Science (OCW). We acknowledge financial support from an NWO-VICI grant. S.S acknowledges funding from the European Union’s Horizon 2020 programme under the Marie Skłodowska-Curie grant agreement No. 656327. We thank A. Wijkamp of the van ’t Hoff Laboratory for Physical and Colloid Chemistry for providing us with fluorescently-labelled polystyrene beads and S. O. Toscano for her help in acquiring experimental results.

Appendix A: Materials & Experimental Methods

1. Particle production & tracking

Polymeric microparticles are produced and observed with an experimental setup, similar to the one used by Uspal *et al.* [1]. Polydimethylsiloxane (PDMS, Sylgard[®] 184, Dow Corning), microfluidic devices are produced according to [30]. A UV-crosslinking oligomer, poly-(ethyleneglycol) diacrylate (PEG-DA $M_n = 700$, $\eta = 55 \times 10^{-3}$ Pa s, Sigma-Aldrich), is mixed with a photoinitiator, hydroxy-2-methylpropiophenone, (Darocur[®] 1173, Sigma-Aldrich), in a 19:1 volume ratio and the mixture is pumped through the microfluidic channel. The device, loaded with prepolymer, is mounted on the stage of a motorized Nikon Ti Eclipse inverted optical microscope. A photolithographic mask with well-defined shape is inserted between the UV light source and the microscope objective. Mask designs are made in Wolfram Mathematica[®] and post-processed in Dassault Systèmes’ DraftSight[®].

Microparticles are produced by shining a 100 ms pulse of UV light through the mask onto the channel, thus confining photopolymerization to a discrete part of the prepolymer mixture. Oxygen, diffusing through the PDMS walls of the device, inhibits crosslinking [30]. This ensures the formation of two lubrication layers, which separate the particle from the z -walls, thus preventing sticking.

The microparticle is set in motion by applying a pressure drop Δp across the channel and tracked by moving the automated stage in a stepwise manner. Since two different microfluidic devices with differing hydraulic resistances were used, the applied pressure differs depending on the device used – $\Delta p_1 = 0.10 \pm 0.01$ psig and $\Delta p_2 = 0.15 \pm 0.01$ psig. Both pressure drops produce a flow with $U_0 \approx 50 \mu\text{m s}^{-1}$ in the respective microfluidic device. The experimental uncertainty in determining U_0 is around 10% [31].

Particle positions and orientations are extracted from the acquired movie using a custom-written MATLAB script, which employs circular Hough transforms to identify the particle shape in each frame. The script utilizes MATLAB's Bio-Formats package [32] and the calcCircle tool.

2. Channel geometry & determination

Both used devices feature a microfluidic channel of length ($L = 11.54 \pm 0.01$ cm) and width ($W = 515 \pm 2 \mu\text{m}$) determined via optical microscopy. The channel height ($H = 30 \pm 1 \mu\text{m}$) is inferred from fluorescent particle tracking [1] and verified with optical and scanning electron microscopy by cutting the device and looking at the cross section. Briefly, fluorescently-labelled polystyrene beads with an average diameter of $1.89 \mu\text{m}$ are introduced in the prepolymer mixture. After focussing in the mid-plane of the channel, the beads are tracked, as the mixture is pumped through the device. Due to optical depth of focus and bead size, a normal distribution of particle velocities is obtained. The mean of the distribution is taken as U_0 and the height of the channel is calculated via Eq. 10. Particle height ($H_p = 25.7 \pm 1.4 \mu\text{m}$) is measured via optical microscopy and is used to calculate the lubrication layer thickness ($h = (H - H_p)/2 = 2.2 \pm 0.9 \mu\text{m}$).

Appendix B: Lorentz reciprocal theorem for Brinkman flow

In this appendix, we derive a version of the Lorentz reciprocal theorem for solutions of the Brinkman equation. Let $\bar{\mathbf{u}}$ and $\bar{\mathbf{u}}'$ be two solutions to the Brinkman equation in a two-dimensional fluid domain A with boundary ∂A , with different boundary conditions. These solutions have corresponding stress tensors $\bar{\sigma}$ and $\bar{\sigma}'$, defined as

$$\bar{\sigma}_{ij} = -\bar{p}\delta_{ij} + \eta H(\partial_i \bar{u}_j + \partial_j \bar{u}_i), \quad (\text{B1})$$

and similarly for $\bar{\sigma}'$. With this definition, we may write the Brinkman equation (11) as

$$\nabla_{2\text{D}} \cdot \bar{\sigma} = \frac{12\eta}{H} \bar{\mathbf{u}}, \quad \nabla_{2\text{D}} \cdot \bar{\mathbf{u}} = 0. \quad (\text{B2})$$

Let us follow the same steps as in the derivation of the original Lorentz reciprocal theorem [20]. First, consider the quantity $\bar{u}'_i(\partial_j \bar{\sigma}_{ij})$, which can be rewritten as

$$\begin{aligned} \bar{u}'_i(\partial_j \bar{\sigma}_{ij}) &= \partial_j(\bar{u}'_i \bar{\sigma}_{ij}) - \bar{\sigma}_{ij} \partial_j \bar{u}'_i = \partial_j(\bar{u}'_i \bar{\sigma}_{ij}) - (-p\delta_{ij} + \eta(\partial_i \bar{u}_j + \partial_j \bar{u}_i)) \partial_j \bar{u}'_i \\ &= \partial_j(\bar{u}'_i \bar{\sigma}_{ij}) - \eta(\partial_i \bar{u}_j + \partial_j \bar{u}_i) \partial_j \bar{u}'_i, \end{aligned} \quad (\text{B3})$$

where the term involving \bar{p} drops out due to the incompressibility constraint $\partial_i \bar{u}'_i = 0$. Interchanging $\bar{\mathbf{u}}$ and $\bar{\mathbf{u}}'$ and subtracting gives us

$$\bar{u}'_i(\partial_j \bar{\sigma}_{ij}) - \bar{u}_i(\partial_j \bar{\sigma}'_{ij}) = \partial_j(\bar{u}'_i \bar{\sigma}_{ij} - \bar{u}_i \bar{\sigma}'_{ij}). \quad (\text{B4})$$

For solutions of Stokes flow, both terms of the left-hand-side of Eq. (B4) vanish identically leading to the Lorentz reciprocal theorem. For solutions of the Brinkman equation, the left-hand-side of Eq. (B4) vanishes because when Eq. (B2) is applied to it, we find

$$\bar{u}'_i \frac{12\eta}{H} \bar{u}_i - \bar{u}_i \frac{12\eta}{H} \bar{u}'_i = 0, \quad (\text{B5})$$

such that Eq. (B4) reads

$$\nabla_{2\text{D}} \cdot (\bar{\mathbf{u}}' \cdot \bar{\sigma} - \bar{\mathbf{u}} \cdot \bar{\sigma}') = 0. \quad (\text{B6})$$

Thus, using the two-dimensional divergence theorem, we obtain the Lorentz reciprocal theorem for Brinkman flow:

$$\oint_{\partial A} ds \bar{\mathbf{u}} \cdot \bar{\sigma}' \cdot \mathbf{n} = \oint_{\partial A} ds \bar{\mathbf{u}}' \cdot \bar{\sigma} \cdot \mathbf{n}, \quad (\text{B7})$$

where ∂A denotes the one-dimensional boundary of the two-dimensional fluid domain A where $\bar{\mathbf{u}}$ and $\bar{\mathbf{u}}'$ are defined and solve the Brinkman equation. Using this relation, symmetry properties of the resistance tensor \mathcal{R}_f defined in (15) for particles in Hele-Shaw cells may be proven, see Appendix C.

Appendix C: Fluid resistance tensor from the Brinkman equation

In this appendix, we show explicitly that the force \mathbf{F}_f and torque T_f exerted on the particle by the (quasi-)two-dimensional Brinkman fluid are related to the particle velocity and angular velocity in terms of a 3×3 resistance tensor \mathcal{R}_f . Inspired by the decompositions into sub-solutions of the original Stokes problem in Section II A, we exploit the linearity of the Brinkman equation to write the solutions as the superpositions $\bar{\mathbf{u}} = \bar{\mathbf{u}}_0 + \bar{\mathbf{u}}' + \bar{\mathbf{u}}''$ and $\bar{p} = \bar{p}_0 + \bar{p}' + \bar{p}''$, where $(\bar{p}_0, \bar{\mathbf{u}}_0)$, $(\bar{p}', \bar{\mathbf{u}}')$ and $(\bar{p}'', \bar{\mathbf{u}}'')$ are solutions to the Brinkman equation (11) with boundary conditions

$$\bar{\mathbf{u}}_0|_{\text{walls}} = 0, \quad \bar{\mathbf{u}}_0|_{\text{inlet}} = U_0 \hat{\mathbf{x}}, \quad \bar{\mathbf{u}}_0|_{r \in \partial \bar{S}_p} = 0; \quad (\text{C1})$$

$$\bar{\mathbf{u}}'|_{\text{walls}} = 0, \quad \bar{\mathbf{u}}'|_{\text{inlet}} = 0, \quad \bar{\mathbf{u}}'|_{r \in \partial \bar{S}_p} = \mathbf{U}_p; \quad (\text{C2})$$

$$\bar{\mathbf{u}}''|_{\text{walls}} = 0, \quad \bar{\mathbf{u}}''|_{\text{inlet}} = 0, \quad \bar{\mathbf{u}}''|_{r \in \partial \bar{S}_p} = \omega_p(-y - y_p, x - x_p), \quad (\text{C3})$$

respectively. Here, $\bar{\mathbf{u}}_0$ corresponds to the situation in which the particle is stationary subject to the imposed external flow, while $\bar{\mathbf{u}}'$ and $\bar{\mathbf{u}}''$ correspond to the situation where the particle is translating and rotating, respectively, in the absence of an imposed flow. The stress tensor of Eq. (13), being linear in the fields $\bar{\mathbf{u}}$ and \bar{p} , admits a similar decomposition $\bar{\sigma} = \bar{\sigma}_0 + \bar{\sigma}' + \bar{\sigma}''$, which is then inherited by the force \mathbf{F}_f and torque T_f via Eq. (14). While the force and torque on the stationary particle follow directly from Eq. (14) by substituting $\bar{\sigma}_0$ for $\bar{\sigma}$, let us consider the contributions from $\bar{\sigma}'$ and $\bar{\sigma}''$ in more detail.

a. Translation

The linearity of the Brinkman equation allows for a factorization

$$\bar{u}'_i = \bar{U}'_{ij} U_{p,j}, \quad \bar{p}' = \eta \bar{\mathcal{P}}'_{ij} U_{p,j}, \quad (\text{C4})$$

where the tensor fields $(\bar{U}', \bar{\mathcal{P}}')$ obey

$$-\partial_i \bar{\mathcal{P}}'_j + \partial_k^2 \bar{U}'_{ij} - \frac{12}{H} \bar{U}'_{ij} = 0, \quad \partial_i \bar{U}'_{ij} = 0, \quad (\text{C5})$$

$$\bar{U}'_{ij}|_{\text{walls}} = \bar{U}'_{ij}|_{\text{inlet}} = 0, \quad \bar{U}'_{ij}|_{r \in \partial \bar{S}_p} = \delta_{ij}, \quad (\text{C6})$$

which lead to the original Brinkman equation for $(\bar{\mathbf{u}}', \bar{p}')$ by contracting with \mathbf{U}_p . In turn, the fields $(\bar{U}', \bar{\mathcal{P}}')$ define a tensor

$$\bar{\Sigma}'_{ijk} = -\delta_{ij} \bar{\mathcal{P}}'_k + \partial_i \bar{U}'_{jk} + \partial_j \bar{U}'_{ik}, \quad (\text{C7})$$

which is related to the stress tensor by $\bar{\sigma}'_{ij} = \eta \bar{\Sigma}'_{ijk} (U_p)_k$. Next, we define

$$\bar{K}_{ik} = - \oint_{\partial \bar{S}_p} dS (\bar{\Sigma}'_{ijk} n_j), \quad (\text{C8})$$

$$\bar{C}'_k = - \oint_{\partial \bar{S}_p} dS \left((x - x_p) (\bar{\Sigma}'_{yjk} n_j) - (y - y_p) (\bar{\Sigma}'_{xjk} n_j) \right), \quad (\text{C9})$$

such that the hydrodynamic force and torque that the two-dimensional fluid exerts on the translating particle are expressed as

$$F'_{f,i} = -\eta \bar{K}_{ij} U_{p,j}, \quad T'_f = -\eta \bar{C}'_j U_{p,j}. \quad (\text{C10})$$

Similar to the the derivation for the three-dimensional resistance tensor, we can prove that the 2×2 tensor K is symmetric, using a version of the Lorentz reciprocal theorem that is proven in Appendix B. Consider the two problems where the particle is either translating with velocity \mathbf{U} or $\tilde{\mathbf{U}}$ through the channel without external flow, with corresponding flow fields $\bar{\mathbf{u}}$ and $\tilde{\bar{\mathbf{u}}}$ that are solutions to the Brinkman equation with boundary conditions (C2). Applying the Brinkman version of the reciprocal theorem, we find

$$\oint_{\partial \bar{S}_p} ds \bar{\mathbf{u}} \cdot \tilde{\bar{\sigma}} \cdot \mathbf{n} + \oint_{\text{w,i,o}} ds \tilde{\bar{\mathbf{u}}} \cdot \bar{\sigma} \cdot \mathbf{n} = \oint_{\partial \bar{S}_p} ds \tilde{\bar{\mathbf{u}}} \cdot \bar{\sigma} \cdot \mathbf{n} + \oint_{\text{w,i,o}} ds \bar{\mathbf{u}} \cdot \tilde{\bar{\sigma}} \cdot \mathbf{n}, \quad (\text{C11})$$

where the integration over ‘w,i,o’ is carried out over the (projected) sidewalls, the inlet and the outlet. However, since both flow fields vanish on the side walls according to Eq. (C2), these integrals vanish identically. Using the no-slip boundary condition on the particle boundary $\partial\bar{S}_p$ and definitions of Eq. (14), we find

$$\tilde{\mathbf{U}} \cdot \mathbf{F}_f = \mathbf{U} \cdot \tilde{\mathbf{F}}_f, \quad (\text{C12})$$

which using Eq. (C10) may be written as

$$\tilde{U}_i \bar{K}_{ij} U_j = U_i \bar{K}_{ij} \tilde{U}_j = \tilde{U}_i \bar{K}_{ji} U_j. \quad (\text{C13})$$

Now, since \mathbf{U} and $\tilde{\mathbf{U}}$ are completely arbitrary, we conclude that \bar{K} is symmetric: $\bar{K}_{ij} = \bar{K}_{ji}$.

b. Rotation

Similarly, we factorize the angular velocity ω_p from the solution $\bar{\mathbf{u}}''$:

$$\bar{u}_i'' = \bar{\mathcal{U}}_i'' \omega_p, \quad \bar{p} = \eta \bar{\mathcal{P}}'' \omega_p, \quad (\text{C14})$$

with (tensor-)fields that obey

$$-\partial_i \bar{\mathcal{P}}'' + \partial_k^2 \bar{\mathcal{U}}_i'' - \frac{12}{H} \bar{\mathcal{U}}_i'' = 0, \quad \partial_i \bar{\mathcal{U}}_i'' = 0, \quad (\text{C15})$$

$$\bar{\mathcal{U}}_i''|_{\text{walls}} = \bar{\mathcal{U}}_i''|_{\text{inlet}} = 0, \quad \bar{\mathcal{U}}_i''|_{(x,y) \in \partial\bar{S}_p} = -y\delta_{ix} + x\delta_{iy}, \quad (\text{C16})$$

which, as usual, lead to the original Brinkman equation for $\bar{\mathbf{u}}''$ with boundary conditions (C3) by multiplying with ω_p . Moreover, we define the tensor $\bar{\Sigma}_{ij}''$, similar to Eq. (C7), which has the property $\bar{\sigma}_{ij}'' = \bar{\Sigma}_{ij}'' \omega_p$. Note that the fields $\bar{\mathcal{U}}''$, $\bar{\mathcal{P}}''$ and $\bar{\Sigma}''$ have dimensions of length of one power higher than their single primed counterparts \mathcal{U}' , \mathcal{P}' and Σ' , while they are of one tensor rank lower, the latter following from the fact that we have only one rotational degree of freedom in two dimensions. To proceed, we define

$$\bar{C}_i'' = - \oint_{\partial\bar{S}_p} dS (\bar{\Sigma}_{ij}'' n_j), \quad (\text{C17})$$

$$\bar{\Omega} = - \oint_{\partial\bar{S}_p} dS (x - x_p) (\bar{\Sigma}_{yj}'' n_j) - (y - y_p) (\bar{\Sigma}_{xj}'' n_j), \quad (\text{C18})$$

such that

$$\mathbf{F}_{f,i}'' = -\eta \bar{C}_i'' \omega_p, \quad T_f'' = -\eta \bar{\Omega} \omega_p. \quad (\text{C19})$$

Similar to proving that \bar{K} is symmetric, we can use the Lorentz reciprocal theorem of Appendix B to prove that in fact $C_i' = C_i''$, but we leave this to the reader.

c. Complete particle motion

Taking together the contributions from the sub-solutions $\bar{\mathbf{u}}_0$, $\bar{\mathbf{u}}'$ and $\bar{\mathbf{u}}''$, we find that the force and torque on the moving particle exerted by the two-dimensional fluid can be written as

$$\begin{pmatrix} \mathbf{F} \\ T \end{pmatrix}_f = -\eta \mathcal{R}_f \begin{pmatrix} \mathbf{U}_p \\ \omega_p \end{pmatrix} + \begin{pmatrix} \mathbf{F}_0 \\ T_0 \end{pmatrix}, \quad (\text{C20})$$

where the components of the 3×3 resistance tensor \mathcal{R}_f are given by

$$\mathcal{R}_f = \begin{pmatrix} \bar{K}_{11} & \bar{K}_{12} & \bar{C}_1 \\ \bar{K}_{12} & \bar{K}_{22} & \bar{C}_2 \\ \bar{C}_1 & \bar{C}_2 & \bar{\Omega} \end{pmatrix}, \quad (\text{C21})$$

with $C_i \equiv C'_i = C''_i$.

-
- [1] William E Uspal, H Burak Eral, and Patrick S Doyle, “Engineering particle trajectories in microfluidic flows using particle shape,” *Nature communications* **4** (2013).
- [2] John Oakey, Robert W Applegate Jr, Erik Arellano, Dino Di Carlo, Steven W Graves, and Mehmet Toner, “Particle focusing in staged inertial microfluidic devices for flow cytometry,” *Analytical chemistry* **82**, 3862–3867 (2010).
- [3] Lisen Wang, Lisa A Flanagan, Noo Li Jeon, Edwin Monuki, and Abraham P Lee, “Dielectrophoresis switching with vertical sidewall electrodes for microfluidic flow cytometry,” *Lab on a Chip* **7**, 1114–1120 (2007).
- [4] Xiaole Mao, Sz-Chin Steven Lin, Cheng Dong, and Tony Jun Huang, “Single-layer planar on-chip flow cytometer using microfluidic drifting based three-dimensional (3d) hydrodynamic focusing,” *Lab on a Chip* **9**, 1583–1589 (2009).
- [5] Daniel R Gossett, Westbrook M Weaver, Albert J Mach, Soojung Claire Hur, Henry Tat Kwong Tse, Wonhee Lee, Hamed Amini, and Dino Di Carlo, “Label-free cell separation and sorting in microfluidic systems,” *Analytical and bioanalytical chemistry* **397**, 3249–3267 (2010).
- [6] Ryan Tewhey, Jason B Warner, Masakazu Nakano, Brian Libby, Martina Medkova, Patricia H David, Steve K Kotsopoulos, Michael L Samuels, J Brian Hutchison, Jonathan W Larson, *et al.*, “Microdroplet-based pcr enrichment for large-scale targeted sequencing,” *Nature biotechnology* **27**, 1025–1031 (2009).
- [7] Mehmet Toner and Daniel Irimia, “Blood-on-a-chip,” *Annu. Rev. Biomed. Eng.* **7**, 77–103 (2005).
- [8] Xiangchun Xuan, Junjie Zhu, and Christopher Church, “Particle focusing in microfluidic devices,” *Microfluidics and nanofluidics* **9**, 1–16 (2010).
- [9] Hyungkook Jeon, Youngkyu Kim, and Geunbae Lim, “Continuous particle separation using pressure-driven flow-induced miniaturizing free-flow electrophoresis (pdf-induced μ -ffe),” *Scientific reports* **6** (2016).
- [10] P Sajeesh and Ashis Kumar Sen, “Particle separation and sorting in microfluidic devices: a review,” *Microfluidics and nanofluidics* **17**, 1–52 (2014).
- [11] Nicole Pamme, “Continuous flow separations in microfluidic devices,” *Lab on a Chip* **7**, 1644–1659 (2007).
- [12] Kerwin Kwek Zeming, Shashi Ranjan, and Yong Zhang, “Rotational separation of non-spherical bioparticles using i-shaped pillar arrays in a microfluidic device,” *Nature communications* **4**, 1625 (2013).
- [13] Weihua Li, Sheng Yan, Ronald Sluyter, Nam-Trung Nguyen, Jun Zhang, and Gursel Alici, “Inertial particle separation by differential equilibrium positions in a symmetrical serpentine micro-channel,” *Scientific Reports* (2014).
- [14] Mahdokht Masaeli, Elodie Sollier, Hamed Amini, Wenbin Mao, Kathryn Camacho, Nishit Doshi, Samir Mitragotri, Alexander Alexeev, and Dino Di Carlo, “Continuous inertial focusing and separation of particles by shape,” *Physical Review X* **2**, 031017 (2012).
- [15] Tsevi Beatus, Roy H Bar-Ziv, and Tsvi Tlusty, “The physics of 2d microfluidic droplet ensembles,” *Physics reports* **516**, 103–145 (2012).
- [16] B Shen, M Leman, M Reyssat, and P Tabeling, “Dynamics of a small number of droplets in microfluidic hele–shaw cells,” *Experiments in Fluids* **55**, 1728 (2014).
- [17] William E Uspal and Patrick S Doyle, “Scattering and nonlinear bound states of hydrodynamically coupled particles in a narrow channel,” *Physical Review E* **85**, 016325 (2012).
- [18] Helene Berthet, Marc Fermigier, and Anke Lindner, “Single fiber transport in a confined channel: Microfluidic experiments and numerical study,” *Physics of Fluids* **25**, 103601 (2013).
- [19] Dhananjay Dendukuri, Daniel C Pregel, Jesse Collins, T Alan Hatton, and Patrick S Doyle, “Continuous-flow lithography for high-throughput microparticle synthesis,” *Nature materials* **5**, 365–369 (2006).
- [20] S Kim and SJ Karrila, 1991, *Microhydrodynamics: Principles and Selected Applications*, Butterworth-Heinemann, Boston.
- [21] John Happel and Howard Brenner, *Low Reynolds number hydrodynamics: with special applications to particulate media*, Vol. 1 (Springer Science & Business Media, 2012).
- [22] L Gary Leal, *Advanced transport phenomena: fluid mechanics and convective transport processes* (Cambridge University Press, 2007).
- [23] Howard Brenner, “The stokes resistance of an arbitrary particle,” *Chemical Engineering Science* **18**, 1–25 (1963).
- [24] Howard Brenner, “The stokes resistance of an arbitrary particle—ii: An extension,” *Chemical Engineering Science* **19**, 599–629 (1964).
- [25] For the remainder of this text, \mathbf{F} and \mathbf{U}_p denote two-dimensional force and particle velocity, respectively.
- [26] HC Brinkman, “A calculation of the viscous force exerted by a flowing fluid on a dense swarm of particles,” *Applied Scientific Research* **1**, 27–34 (1949).
- [27] William E Uspal and Patrick S Doyle, “Self-organizing microfluidic crystals,” *Soft matter* **10**, 5177–5191 (2014).
- [28] D Halpern and Timothy W Secomb, “Viscous motion of disk-shaped particles through parallel-sided channels with near-minimal widths,” *Journal of Fluid Mechanics* **231**, 545–560 (1991).
- [29] See the ancillary files of this preprint for the animations and microscopic movie of a reorienting dumbbell particle. Descriptions of these animations are found below in the Supplemental material.
- [30] Dhananjay Dendukuri, Priyadarshi Panda, Ramin Haghgooei, Ju Min Kim, T. Alan Hatton, and Patrick S. Doyle, “Modeling of oxygen-inhibited free radical photopolymerization in a pdms microfluidic device,” *Macromolecules* **41**, 8547–8556 (2008).

- [31] See Supplemental Material at [URL will be inserted by publisher] for detailed calculation of all reported experimental uncertainties.
- [32] Melissa Linkert, Curtis T Rueden, Chris Allan, Jean-marie Burel, Will Moore, Andrew Patterson, Brian Loranger, Josh Moore, Carlos Neves, Donald Macdonald, Aleksandra Tarkowska, Caitlin Sticco, Emma Hill, Mike Rossner, Kevin W Eliceiri, and Jason R Swedlow, “Metadata matters : access to image data in the real world,” *The Journal of Cell Biology* **189**, 777–782 (2010).

Supplemental material: Calculating the motion of highly confined, arbitrary-shaped particles in Hele-Shaw channels

DESCRIPTION OF THE MOVIES

Here, we give a short description of the experimentally-obtained movie and the animations provided as supplementary information. Definitions of the shape parameters, the channel dimensions and other parameters may be found in the main text.

- M1** Movie 1 is obtained from microscopic images and shows a dumbbell particle with $R_1/R_2 = 2$ rotating towards a stable orientation with the large disk upstream, while translating in the positive x -direction (to the right), along with the externally imposed flow. The field of view of the microscope follows the particle in a stepwise manner.
- A1** Animation 1 shows a reorienting dumbbell particle with $R_1/R_2 = 2$, as seen from a fixed (laboratory) frame. The color of the heat map indicates the magnitude of the flow field \mathbf{u} in units of U_0 .
- A2** Animation 2 shows again a reorienting dumbbell particle with $R_1/R_2 = 2$, now seen from a frame co-moving with the particle. The arrows indicate the disturbance flow field $\bar{\mathbf{u}} - \bar{\mathbf{u}}_0$, where $\bar{\mathbf{u}}_0$ is the externally imposed flow field far away or in the absence of the particle. The colors of the arrows correspond to the magnitude $|\bar{\mathbf{u}} - \bar{\mathbf{u}}_0|$ of the disturbance flow field.
- A3** Animation 3 shows again a reorienting dumbbell particle with $R_1/R_2 = 2$, seen from a frame co-moving with the particle, now shown with isobars of the disturbance pressure field $p - p_0$, in units of $\eta U_0/H$. Here, p_0 denotes the externally imposed pressure field far away from the particle.

DETERMINATION OF EXPERIMENTAL UNCERTAINTY

To calculate the experimental uncertainty in determining the scaled rotation time $\tilde{\tau} = \tau U_0/H$ and the time evolution of the particle orientation with respect to the flow $\theta(t)$, we carry out an error propagation analysis. In the general case of an experimental quantity F dependent on a series of experimentally-determined quantities $\{x_i\}$ with uncertainties $\{\sigma_{x_i}\}$, one calculates the uncertainty in F as:

$$\sigma_F = \sqrt{\sum_{\{x_i\}} \left(\frac{\partial R(\{x_i\})}{\partial x_i} \sigma_{x_i} \right)^2}. \quad (\text{S1})$$

1. Uncertainty in the particle thickness

The thickness of the particles, $H_p = H - 2h$, is measured at the outlet, where they topple over. The particles are observed from the side and the distance between the edges of the top and bottom face is calculated. Due to uneven illumination of the faces and low contrast of the system, the edges appear thicker than one pixel, therefore a type B uncertainty should be taken into consideration. Type B uncertainty reflects the random nature of a process and any human bias in measuring it. Since most observed edges are roughly 5 pixels thick, a type B uncertainty σ_B of 3 pixels is estimated.

The finite spacial resolution of the microscope used suggests a type A uncertainty, as well, which is estimated to be the size of a single pixel at 40x magnification with 2-by-2 pixel binning - $\sigma_A = 0.323 \mu\text{m}/\text{px}$. The total uncertainty in determining the position of a given edge is a product of σ_A and σ_B and amounts to roughly a micron.

To determine the uncertainty in the thickness, we use Eq. 1, in which $F(\{x_i\}) = H_p(z_1, z_2) = z_1 - z_2$ and $\sigma_{z_1} = \sigma_{z_2} = 1 \mu\text{m}$:

$$\sigma_{H_p} = \sigma_{z_1} \sqrt{2} = 1.4 \mu\text{m} \quad (\text{S2})$$

The thickness of 20 cylinders, produced in the microfluidic device, is measured. An average thickness $\langle H_p \rangle = 25.7 \mu\text{m}$ and sample standard deviation $s = 0.3 \mu\text{m}$ is calculated. The minimum and maximum values are $H_{p,\text{min}} = 25.0 \pm 1.4 \mu\text{m}$ and $H_{p,\text{max}} = 26.1 \pm 1.4 \mu\text{m}$. Since the uncertainty in the measurements is greater than the sample standard deviation, we report $\langle H_p \rangle = 25.7 \pm 1.4 \mu\text{m}$.

2. Uncertainty in the channel height

To determine the channel height using optical microscopy, the microfluidic chip is cut with a razor and the cross section is viewed. The type B uncertainty in this case is 2 pixels since the channel edges are sharper than those of PEG-DA particles. The type A uncertainty remains the size of a single pixel. Following the same approach like in the previous case, an uncertainty $\sigma_H = 2 \times 0.323\sqrt{2} = 0.9 \mu\text{m}$ is calculated.

3. Uncertainty in the average flow velocity

Obtaining the mean flow velocity requires fluorescent particle tracking in which a video of fluorescent beads flowing through the channel is recorded. The positions of a given particle in two consecutive frames are compared and the path length is calculated as their difference. Similarly to the uncertainties in channel and particle height, the uncertainty in the flow velocity scales linearly with the length-to-pixel ratio of the lens used and the uncertainty in determining the center of a given particle. The particle tracking algorithm uses a weighted centroid method to calculate the particle center, which has sub-pixel accuracy. We will make a non-conservative estimate and limit the type B uncertainty to half a pixel. Then, the uncertainty in the distance traveled by any particle over two consecutive frames is $\sigma_{\Delta x} = 0.323/2\sqrt{2} = 0.23 \mu\text{m}$. The frame rate of the movie is 20 FPS, therefore the lag between two consecutive frames is $t_f = 0.05 \text{ s}$. Applying Eq. 1 to the expression for the particle velocity $v_p = \Delta x/t_f$ yields:

$$\sigma_{v_p} = \frac{\sigma_{\Delta x}}{t_f} = 4.6 \mu\text{m s}^{-1} \quad (\text{S3})$$

4. Uncertainty in the disk position in a dumbbell

The uncertainty in determining where the center of a disk within a dumbbell lies is governed by the spacial resolution of the microscope and the accuracy of the numerical algorithm used to detect the disks. While tracking dumbbells, we use a 20x lens with 2-by-2 pixel binning, which results in a distance-to-pixel ratio of $0.650 \mu\text{m}/\text{px}$. The circular Hough transform we use to detect the disks utilizes a weighted centroid method, which reports the coordinates of the disk center with a sub-pixel accuracy. However, the algorithm reports radii with a resolution of 1 pixel. Therefore, we estimate an uncertainty of 1 pixel or $0.650 \mu\text{m}$ in determining the disk coordinates.

5. Uncertainty in the shaft length in a dumbbell

Although the center-to-center distance of the two disks is fixed, there is both type A and type B uncertainty in its determination. We discussed the type A uncertainty in the previous section. The type B uncertainty stems from the randomness of the photopolymerization reaction – different particles have slightly different shaft lengths. To estimate the uncertainty in the length of the shaft, we write the expression for it explicitly and apply Eq. 1 to it:

$$|\mathbf{O}(t)| = l = \sqrt{O_x^2(t) + O_y^2(t)} = \sqrt{(x_S(t) - x_B(t))^2 + (y_S(t) - y_B(t))^2}. \quad (\text{S4})$$

$$\begin{aligned} \sigma_l &= \sqrt{\left(\frac{\partial l}{\partial x_S} \sigma_{x_S}\right)^2 + \left(\frac{\partial l}{\partial x_B} \sigma_{x_B}\right)^2 + \left(\frac{\partial l}{\partial y_S} \sigma_{y_S}\right)^2 + \left(\frac{\partial l}{\partial y_B} \sigma_{y_B}\right)^2} \\ &= \sqrt{\frac{2(x_S(t) - x_B(t))^2 \sigma_{x_S}^2}{l^2} + \frac{2(y_S(t) - y_B(t))^2 \sigma_{y_S}^2}{l^2}} \\ &= \sqrt{\frac{2\sigma_{x_S}^2}{l^2}} l = \sigma_{x_S} \sqrt{2} = 0.9 \mu\text{m}. \end{aligned} \quad (\text{S5})$$

6. Uncertainty in the orientation angle

The orientation angle of the microparticle $\theta(t)$ is calculated from the vector $\mathbf{O}(t)$, which starts from the center of the big disk of a dumbbell and ends in the center of the small disk:

$$\theta(t) = \arccos\left(\frac{\mathbf{O}(t) \cdot \mathbf{e}_0}{|\mathbf{O}(t)||\mathbf{e}_0|}\right) = \arccos\left(\frac{O_x(t)}{|\mathbf{O}(t)|}\right) = \arccos\left(\frac{O_x(t)}{\sqrt{O_x^2(t) + O_y^2(t)}}\right), \quad (\text{S6})$$

where \mathbf{e}_0 is the unit vector aligned with the flow velocity. It is made sure the channel is leveled in such a way that the flow direction is parallel to the x -coordinate of the field of view. This reduces the dot product of the two vectors to the x -component of $\mathbf{O}(t)$. Applying Eq. 1 to Eq. 6 yields:

$$\begin{aligned} \sigma_\theta &= \sqrt{\left(\frac{\partial\theta}{\partial x_S}\sigma_{x_S}\right)^2 + \left(\frac{\partial\theta}{\partial x_B}\sigma_{x_B}\right)^2 + \left(\frac{\partial\theta}{\partial y_S}\sigma_{y_S}\right)^2 + \left(\frac{\partial\theta}{\partial y_B}\sigma_{y_B}\right)^2} \\ &= \sqrt{2\frac{\sigma_{x_S}^2}{l^2}} = \frac{\sigma_{x_B}}{l}\sqrt{2} = 0.84^\circ. \end{aligned} \quad (\text{S7})$$

We make a non-conservative estimate and round the uncertainty in the orientation angle up to 1° .

7. Uncertainty in the characteristic rotation time τ

The rotation time is easily accessible numerically via the rotation velocity at $\theta = \pi/2$. Experimentally, however, this is not a viable option because this would mean estimating τ from only two micrographs with great uncertainty. To obtain a statistically-significant result experimentally, we fit the time evolution of the orientation angle to an analytical expression for $\theta(t)$. Solving Eq. 28 in the main text by making the substitution $\sin(\theta) = 2x/(1+x^2)$ yields:

$$-\frac{t}{\tau} = \ln\left(\frac{\tan(\theta/2)}{\tan(\theta_0/2)}\right). \quad (\text{S8})$$

Rearranging, we obtain the equation in linear form:

$$\ln(\tan(\theta/2)) = \ln(\tan(\theta_0/2)) - \frac{1}{\tau}t. \quad (\text{S9})$$

We calculate τ from the slope of a line fitted to a dataset $[t, \ln(\tan(\theta/2))]$. The estimated slope has an uncertainty since the data cannot be perfectly fitted to a line. The uncertainty in the slope b is inversely proportional to the square root of the number of data points N used in the linear regression:

$$\sigma_b = b\frac{1}{\sqrt{N-2}}\sqrt{\frac{1}{R^2} - 1}, \quad (\text{S10})$$

where R^2 reflects the goodness of the fit. In our experiments the relative uncertainty in the slope is less than 1.5% due to:

1. the great number of images we record – each experimental movie consists of at least 600 frames.
2. the high R^2 value – in all experiments $R^2 > 0.980$.

8. Uncertainty in the scaled rotation time $\tilde{\tau}$

Applying Eq. 1 to the scaled rotation time $\tilde{\tau} = \tau U_0/H$ yields:

$$\begin{aligned} \sigma_{\tilde{\tau}} &= \sqrt{\frac{U_0^2}{H^2}\sigma_\tau^2 + \frac{\tau^2}{H^2}\sigma_{U_0}^2 + \frac{U_0^2\tau^2}{H^4}\sigma_H^2} \\ &= \sqrt{\tilde{\tau}^2\frac{\sigma_\tau^2}{\tau^2} + \tilde{\tau}^2\frac{\sigma_{U_0}^2}{U_0^2} + \tilde{\tau}^2\frac{\sigma_H^2}{H^2}} \\ &= \tilde{\tau}\sqrt{\frac{\sigma_\tau^2}{\tau^2} + \frac{\sigma_{U_0}^2}{U_0^2} + \frac{\sigma_H^2}{H^2}} \end{aligned} \quad (\text{S11})$$

The three relative uncertainties are $\sigma_\tau/\tau \simeq 1\%$, $\sigma_{U_0}/U_0 \simeq 10\%$ and $\sigma_H/H = 3\%$. Filling in these numbers in Eq. 11 yields a relative uncertainty in $\tilde{\tau}$ of roughly 11% – the uncertainty is entirely dominated by the uncertainty in U_0 .